Coordination Chemistry Reviews 253 (2009) 1202–1218

Contents lists available at ScienceDirect

Coordination Chemistry Reviews

journal homepage: www.elsevier.com/locate/ccr

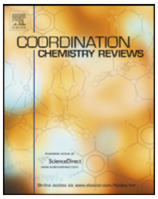

Review

The molecular and electronic structure of carbon–hydrogen bond activation and transition metal assisted hydrogen transfer

Benjamin Alan Vastine, Michael B. Hall*

Department of Chemistry, Texas A&M University, College Station, TX 77843, United States of America

Contents

ARTICLE INFO

Article history:
Received 13 February 2008
Accepted 24 July 2008
Available online 3 August 2008

Keywords:
C–H bond activation
Hydrogen transfer
Bader's analysis
Bonding patterns

ABSTRACT

Following the optimization of the geometry by density functional theory (DFT), we analyze midpoint species along the reaction coordinate for hydrogen transfer in the reaction $R'–H + M–R \rightarrow R–H + M–R'$ with Bader's "Atoms in Molecules" (AIM) analysis. The two "classic" mechanisms for hydrogen transfer, σ-bond metathesis (σBM) and oxidative addition/reductive elimination (OA/RE), are well represented by the reaction of CH_4 with $[Cp_2ScCH_3]$ and $[CpIr(PH_3)(CH_3)]^+$, respectively ($Cp = \eta^5\text{-}C_5H_5$). The midpoint species for these two pathways are the transition state $[Cp_2Sc(CH_3)_2H]^‡$ and the OA intermediate, $[CpIr(PH_3)(CH_3)_2H]^+$. Bond (B) critical points (CP) were located along the Sc–C and C–H coordinates of the four-center geometry of $[Cp_2Sc(CH_3)_2H]^‡$; a ring (R) CP was located in the center. For the intermediate $[CpIr(PH_3)(CH_3)_2H]^+$, bond critical points (BCPs) were located only along the Ir–C and Ir–H coordinates of the four-center geometry. Most of the new mechanisms that have been proposed are characterized by single transition states with short M–H distances connecting reactants with products. Representative models of a variety of alternative mechanisms were analyzed; in all, seven

---

* Corresponding author. Tel.: +1 979 845 1843; fax: +1 979 845 6077.
E-mail address: hall@science.tamu.edu (M.B. Hall).

doi:10.1016/j.ccr.2008.07.015

different bonding patterns were identified that describe seven unique mechanisms for hydrogen transfer. In general, those metal centers that have d electrons available to participate in hydrogen transfer interact with the transferring hydrogen during this reaction as the hydrogen atom is nearly unique in being able to support omni-directional bridging bonds. Basis sets and density functional effects were investigated with $[Cp_2Sc(CH_3)_2H]^‡$ as the model. Seventeen basis sets were assigned to scandium and the densities at the Sc–C BCP increased slightly up to the quadruple-ζ level in the basis. The densities at the C–H BCPs are constant, but the densities at the ring critical point (RCP) also increased slightly. Ten density functionals were tested and the densities at the BCPs and RCP are constant, but the Sc–C BCP moved slightly farther from the scandium as the amount of exact exchanged admixed into the functional increased.

1. Introduction

The activation of the carbon–hydrogen (C–H) bond is an area of high interest in chemical research [1]. Transition metals (TM) are especially suited for the facile activation of these bonds because the metal d orbitals possess the proper energies and symmetries that match the C–H bonding (σ) and antibonding (σ*) orbitals [2]. When coordinating to the metal, the filled C–H σ orbital donates electron density to an unoccupied d orbital, and a filled metal orbital (if available) donates electron density to the empty C–H σ* orbital; both the "forward" and "back" donation weaken the C–H bond and in some cases causes scission. Upon activation, the hydrogen can be transferred to a pendant ligand.

Historically two "classic" mechanisms have been assumed for C–H activation and hydrogen transfer: (1) σ-bond metathesis (σBM) [3] and (2) oxidative addition/reductive elimination (OA/RE) [4]. The reaction profiles for these two mechanisms are sketched in Scheme 1. For σBM, only one transition state (TS) is found along the reaction coordinate that joins the reactant and product. This TS represents the midpoint along the reaction coordinate. However, for the OA/RE pathway, an oxidized intermediate (INT) is found at the midpoint along this pathway and two TSs are found on either side of the INT. In the first TS, the R′–H bond is breaking and the M–R′ and M–H bonds are forming; because the metal must use two of its previous nonbonding d electrons in forming these two new bonds, the resulting INT is in a higher formal oxidation state ($n+2$). In the second TS, the M–R and M–H bonds are breaking and the R–H bond is forming; loss of R–H completes the hydrogen transfer. Geometrically, the σBM TS is characterized by a four-center geometry with a long M–H distance (~2.0 Å) and a small R–M–R′ angle (~90°); conversely, the geometry of the oxidized INT is characterized by a short M–H distance (~1.5 Å) and a large R–M–R′ angle (~130°). Representative systems for hydrogen transfer that proceed by the σBM and OA/RE mechanisms are the reaction of CH_4 with $[Cp_2Sc(CH_3)]$ and $[CpIr(PH_3)(CH_3)]^+$ ($Cp = \eta^5\text{-}C_5H_5$), respectively.

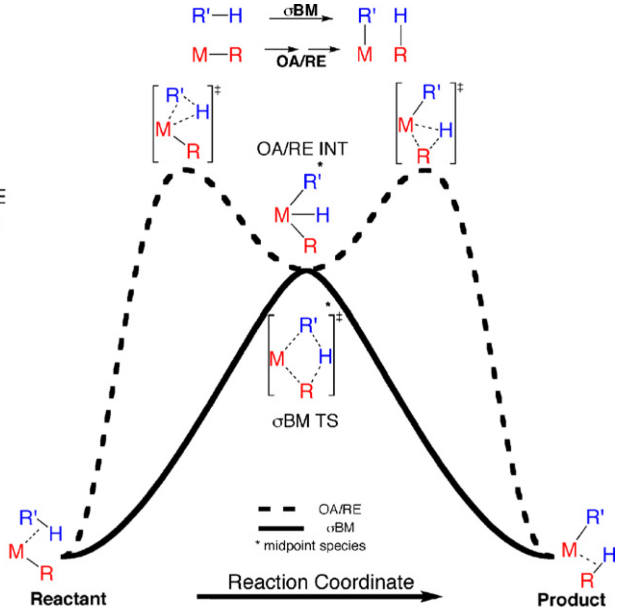

Scheme 1.

Very recently several alternatives to these two classic mechanisms have been proposed. In these alternative mechanisms, a single TS connects reactant and product, but rather than the expected long, nonbonding M–H distance, the midpoint TSs show a short M–H distance. Furthermore, the R′–M–R angle is wider than expected for σBM, the classic mechanism with a single TS. Thus, these systems have a TS that geometrically resembles the OA/RE INT.

Hall, Hartwig and their coworkers [5] investigated the borylation of alkanes with model systems involving the addition of CH_4 to $[CpM(CO)_nBR_2]$ ($M = Fe$, $n = 1$; $M = W$, $n = 2$; $R = OCH_2$). A single TS for C–H and B–H coupling/decoupling connects the σ-bound methane reactant and σ-bound borane product, a result that would imply a σBM type mechanism. However, the short calculated M–H distances (~1.5 Å) and orbitals localized along these coordinates suggest a bonding interaction between the metal the transferring hydrogen. These workers called this new mechanism "metal-assisted σBM″ (MAσBM).

Lin and coworkers, studying the mechanism for hydrogen transfer by the addition of RH ($R = C_6H_5$, $CH_2CH_2OC_2H_5$, CH_3) to $[TpRu(PH_3)(H)]$ [6], found a single seven-coordinate, Ru^{IV} TS connecting the σ-bound alkyl reactant and σ-bound H_2 product. In the related TS, $[TpRu(PH_3)(CH_3)_2H]^‡$, electron density was localized along the Ru–C and Ru–H coordinates but not along the C–H coordinates [7]. Thus, it would appear that the transferring hydrogen interacts only with the metal in this TS. Because of the oxidative character of the TS, these workers called this mechanism an "oxidatively added transition state" (OATS) [8].

Oxgaard et al. [9] investigated the mechanism for the arylation of olefin catalyzed by iridium [10] and ruthenium [11] systems. In particular, the TSs for hydrogen transfer between the phenyl and ethylbenzene ligands in these systems, $[(acac)_2Ir(C_6H_5)(CH_2CH_2Ph)H]^‡$ and $[TpRu(CO)(C_6H_5)(CH_2CH_2Ph)H]^‡$, geometrically resembled seven-coordinate Ir^V and Ru^{IV} intermediates, respectively. The M–H distances were short (~1.5 Å), and the distances between the aryl and alkyl ligands and the transferring hydrogen were considered too long for C–H interactions. Because of these geometric parameters, these researchers also recognized that the transferring hydrogen interacts with the metal in the TS and proposed the name "oxidative hydrogen migration" (OHM).

Finally, Perutz and Sabo-Etienne proposed the name "σ-complex-assisted metathesis" (σ-CAM) [12] mechanism to describe an overall mechanism that includes hydrogen transfer and R–R′ cross-coupling steps, and applied this view to several systems mentioned above. In this mechanism, the reactant and product include σ-bound ligands [13], which promote this close proximity between the transferring hydrogen and the metal.

Our research into these mechanisms has culminated with the characterization of these reaction path midpoint species by their bonding patterns as defined by Bader's "Atoms in Molecules" (AIM) analysis [14]. Because of the lack of separation of steric and bonding effects, geometric parameters by themselves are insufficient for characterizing the connectivity in these species. In the AIM analysis, the electron density is analyzed without recourse to any specific orbital description. Critical points (CP) are located in the electron density and their characteristics can identify bonding and nonbonding sites. By applying this analysis to representative species for the σBM, OA/RE, and alternative mechanisms described above, we proposed a spectrum of mechanisms for metal-mediated hydrogen transfer [15]. Various bonding patterns were identified that described different degrees of connectivity in non-equilibrium species for hydrogen transfer, and the patterns were "resolved" into a spectrum that represents a nearly continuous set of mechanisms.

Here, we expand on our prior work by considering more systems for hydrogen transfer. A wider range of connectivity in midpoint species for hydrogen transfer is identified, which expands the number of mechanisms for hydrogen transfer. We identify seven sets of bonding patterns, five of which lie in between those that are characteristic of the σBM TS and the OA/RE INT. Lastly, we examine the effects of basis sets and density functionals on the bonding patterns.

1.1. Theory of Bader's "Atoms in Molecules" analysis

In Bader's analysis, the charge density ($\rho(\mathbf{r})$) of a given molecule, which is a physical-observable, is analyzed for CPs in the electron density. The location of a CP is denoted by the position vector, $\mathbf{r}_c$, and at these points the first derivative of the density vanishes ($\nabla\rho(\mathbf{r}_c)=0$); therefore, these points can be minima, maxima, or saddle points in the density. The charge density of a molecule is three-dimensional, so there are three curvatures at a CP, which is the rank (ω) of the CP. Through the Hessian matrix ($\boldsymbol{A}(\mathbf{r}_c)$ Eq. (1)), which is a (3 × 3) matrix of the second derivatives of the density with respect to the coordinates ($\delta^2\rho/\delta q\delta q'$), the curvatures at a given CP are represented as

$$\boldsymbol{A}(\mathbf{r}_c)=\begin{pmatrix} \dfrac{\partial^2\rho}{\partial x^2} & \dfrac{\partial^2\rho}{\partial x\partial y} & \dfrac{\partial^2\rho}{\partial x\partial z} \\ \dfrac{\partial^2\rho}{\partial y\partial x} & \dfrac{\partial^2\rho}{\partial y^2} & \dfrac{\partial^2\rho}{\partial y\partial z} \\ \dfrac{\partial^2\rho}{\partial z\partial x} & \dfrac{\partial^2\rho}{\partial z\partial y} & \dfrac{\partial^2\rho}{\partial z^2} \end{pmatrix} \tag{1}$$

Diagonalization of the Hessian matrix ($\boldsymbol{\Lambda}$ Eq. (2)) yields three eigenvalues ($\lambda_1\ \lambda_2\ \lambda_3$) whose sum of signs is the signature (σ) of the CP; as such, the CPs are denoted by their rank and signature as (ω, σ). The reference coordinates, x', y', and z', are those for which the off-diagonal elements of $\boldsymbol{A}(\mathbf{r}_c)$ are zero.

$$\boldsymbol{\Lambda}=\begin{pmatrix} \dfrac{\partial^2\rho}{\partial x'^2} & 0 & 0 \\ 0 & \dfrac{\partial^2\rho}{\partial y'^2} & 0 \\ 0 & 0 & \dfrac{\partial^2\rho}{\partial z'^2} \end{pmatrix}=\begin{pmatrix} \lambda_1 & 0 & 0 \\ 0 & \lambda_2 & 0 \\ 0 & 0 & \lambda_3 \end{pmatrix} \tag{2}$$

For example, the result of this analysis for an atomic center, at which the electron density is a maximum, gives three eigenvalues that are negative in character; therefore, curvatures at atoms have a rank of 3 and a signature of −3 and are therefore labeled as (3, −3) CPs. There are three other possibilities for the signatures of rank 3 CPs, which include:

- (3, −1): two negative eigenvalues; one positive
- (3, +1): one negative eigenvalue; two positive
- (3, +3): all three eigenvalues positive

The (3, −1) CP is called a bond critical point (BCP) because it connects trajectories in the gradient field of the density that originate at two adjacent atoms connected by a chemical bond. Physically, this CP is minimum in the density along the direction connecting the two atoms but a maximum in each of the two orthogonal directions. In other words, there is a local concentration of electron density (perpendicular to the bond) at this critical point, a feature characteristic of a chemical bond. The (3, +1) CP is termed a ring critical point (RCP) because these CPs are located inside a ring of atoms that are linked together by a series of BCPs. Here, the density is a minima in the two orthogonal directions in the "plane" of the ring and a maximum in the direction perpendicular to this "plane". A cage critical point (3, +3), which is a minima in all three orthogonal directions, is located in the density when a ring is capped by one or more atoms.

2. Computational method

All density functional theory [16] (DFT) calculations were performed with the Gaussian 03 suite of programs [17]. Unless otherwise noted, geometries were optimized at the B3LYP/DZP level of theory, and the basis set is described below. The analytical frequencies were calculated for all species; intermediates are characterized by real frequencies and TSs by one imaginary frequency. The B3LYP density functional is comprised of the Becke3 exchange [18] and Lee–Yang–Parr (LYP) correlation [19] functionals, respectively. All 3D geometric and bonding pattern representations were constructed with JIMP2 visualization software [20]. The electron densities of these species were analyzed with the implementation of Bader's analysis in AIM2000 [21]. In the following representations, BCPs and RCPs are marked by red (dark) and yellow (pale) dots, respectively. The bond paths are approximate and represented by dashed lines.

In the DZP basis set, the TM was assigned the Los Alamos National Laboratory 2 (LANL2) effective core potential (ECP) of Hay and Wadt [22] for the core electrons and the (341/341/n1) (Sc → Cu: $n=4$; Y → Ag: $n=3$; La → Au: $n=2$) double-ζ basis set as modified by Couty and Hall [23] (mDZ) for the electrons considered explicitly. One f-polarization function was added to this basis set. The first and second row atoms that interact directly with the TM were assigned the correlation consisted double-ζ basis set (cc-pVDZ) of Dunning [24]. Those atoms that do not interact with the metal were assigned the full double-ζ D95 basis set of Dunning [25]. For **1**, **2**, and **3**, the cc-pVDZ basis sets were augmented with diffuse functions in the optimization and frequency calculations. These assignments are listed explicitly for each species in the Supporting Information. For those species optimized at the TPSS/TZP level of theory, the basis set (TZP) is as follows: iridium was assigned the Stuttgart Relativistic Small Core (RSC) 1997 ECP (SDD) for the inner 60 electrons and the (311111/22111/411) basis set for the 17 explicit electrons [26]; all atoms that touch the metal were assigned the cc-pVTZ basis set [24]; the remaining carbon and hydrogen atoms were assigned the D95 basis set [25].

In the AIM analyses, the ECP/BS that was assigned to the metal was replaced with the well-tempered basis set (WTBS) to reintroduce the core electrons and create an all-electron model [27]. For **1**, **2**, and **3**, the diffuse functions that were added to the cc-pVDZ basis sets were not used. All other assignments of the DZP basis set remained the same.

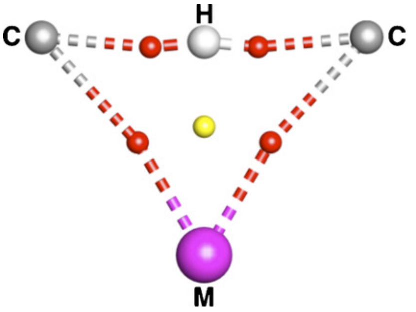

Fig. 1. Characteristic bonding patterns of $[Cp_2M(CH_3)_2H]^‡$ (M = Sc (**1**), Y (**2**), La (**3**)), a typical σBM TS. BCPs were located along the M–C and C–H coordinates, and a RCP was located inside the M–C–H–C coordinates.

An analysis of this procedure and the robustness of the CP results was made for the scandium model (**1**) where the basis sets are as follows: Pople's STO-*n*G (*n* = 3, 6) [28], 3-21G [29], 6-31G with and without an f-polarization function [30]; Huzinaga's WTBS [27]; Ahlrich's pVDZ [31], TZV [32], VDZ [31], VTZ [32], and TZVPP [33]; Peterson's cc-pVDZ, aug-cc-pVDZ, cc-pVDZ-DK, cc-pVTZ, and cc-pVQZ [34], Wachters+f [35], and Bauschlicher's ANO [36]. The density functionals that were used in the same section are as follows: exchange: Becke88 (B) [37], Becke3 (B3) [18], Becke Half&Half (BH&H) [38], modified Perdew–Wang 91 (mPW) [39]; correlation: Lee–Yang–Parr [19], Perdew–Yang 91 (PW91) [39b], Becke95 (B95) [40]; exchange/correlation: Perdew–Burke–Ernzerhof (PBE) [41], Tao–Perdew–Staroverov–Scuseria (TPSS) [42]; stand-alone: MPW-LYP1M [43]. The hybrid versions of the mPWPW91 (MPW0) [39] and PBE (PBE0) [41] functionals were also used in this analysis.

3. Results and discussion

3.1. *The two "classic" mechanisms: σBM and OA/RE*

The "classic" σBM and OA/RE mechanisms have been theoretically investigated by methane reacting with $[Cp_2MCH_3]$ (M = Sc, Y, La) and to $[Cp^*Ir(PR_3)(C'H_3)]^+$ (R = H, Me), respectively, as models closely related to the experimental systems [3,4,15].

Table 1
Metric and AIM data of $[Cp_2M(CH_3)_2H]^‡$ (M = Sc (**1**), Y (**2**), La (**3**))

M	M–C		C–H		$\mathbf{r}^a$ (M–H)	$\rho(\mathbf{r})^b$ (RCP)	∠C–M–C^c
	$\mathbf{r}^a$	$\rho(\mathbf{r})^b$ (BCP)	$\mathbf{r}^a$	$\rho(\mathbf{r})^b$ (BCP)			
Sc (**1**)	2.41	0.049	1.44	0.128	1.90	0.046	73.5
Y (**2**)	2.54	0.047	1.45	0.125	2.05	0.043	69.7
La (**3**)	2.73	0.038	1.44	0.128	2.23	0.035	64.6

[a] Distances in angstroms.
[b] Densities in e/bohr^3.
[c] Angles in degrees.

3.1.1. *CH_4 + $[Cp_2MCH_3]$*

The characteristic bonding patterns for the four-centered geometry (M–C–H–C) of the σBM TSs, $[Cp_2M(CH_3)_2H]^‡$ (M = Sc (**1**), Y (**2**), La (**3**)), are presented in Fig. 1. BCPs are located along both M–C and C–H coordinates and a RCP inside the M–C–H–C coordinates. In Table 1 the optimized geometric parameters and density at the CPs are reported for **1**, **2**, and **3**. As the metal is replaced with the heavier congeners, the M–C and M–H distances increase and the C–M–C angle decreases, while the C–H distances remain essentially unchanged. The bonding patterns of **1**, **2**, and **3** are essentially the same; however, the density at the M–C, C–H BCPs and RCPs decrease, remain unchanged, and decrease down the period, respectively.

To study the OA/RE mechanism, the σ-complexes, TSs, and oxidized INTs along the reaction coordinates for methane addition to $[CpIrPH_3(C'H_3)]^+$ and $[(acac)_2Ir(C'H_3)]$ (acac = acetylacetonate) were studied. The geometric parameters and bonding patterns of $[CpIrPH_3(\sigma\text{-}CH_4)(C'H_3)]^+$ (**4**), $[[CpIrPH_3(CH_3)(C'H_3)H]^+]^‡$ (**5**), and $[CpIrPH_3(CH_3)(C'H_3)H]^+$ (**6**) are presented in Fig. 2. Likewise, the results of similar analyses for $[(acac)_2Ir(\sigma\text{-}CH_4)(C'H_3)]$ (**7**), $[(acac)_2Ir(CH_3)(C'H_3)H]^‡$ (**8**), and $[(acac)_2Ir(CH_3)(C'H_3)H]$ (**9**) are shown in Fig. 3. At the B3LYP/DZP level of theory, we were unable to locate σ-complexes with the Cp* (Cp* = η^5-C_5Me_5) and PMe_3 ligands. However, the σ-complexes, $[CpIrPMe_3(CH_4)(C'H_3)]$ and $[Cp^*IrPH_3(CH_4)(C'H_3)]$, were located at the TPSS/TZP level of theory, but the σ-complex $[Cp^*IrPMe_3(CH_4)(C'H_3)]$ was not located even at this higher level. As a result, we considered the Cp/PH$_3$ species for our full analysis.

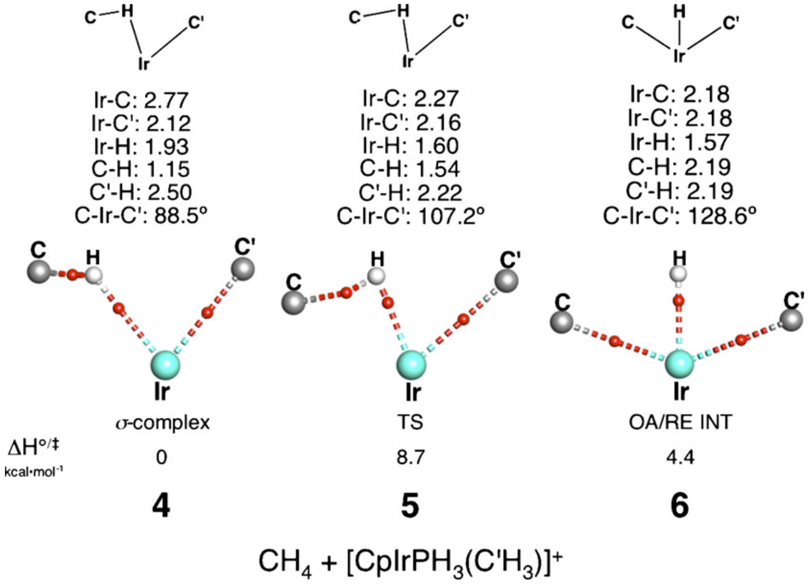

Fig. 2. Optimized geometric parameters and bonding patterns of **4**–**6**. The distances listed are in angstroms and the angles in degrees.

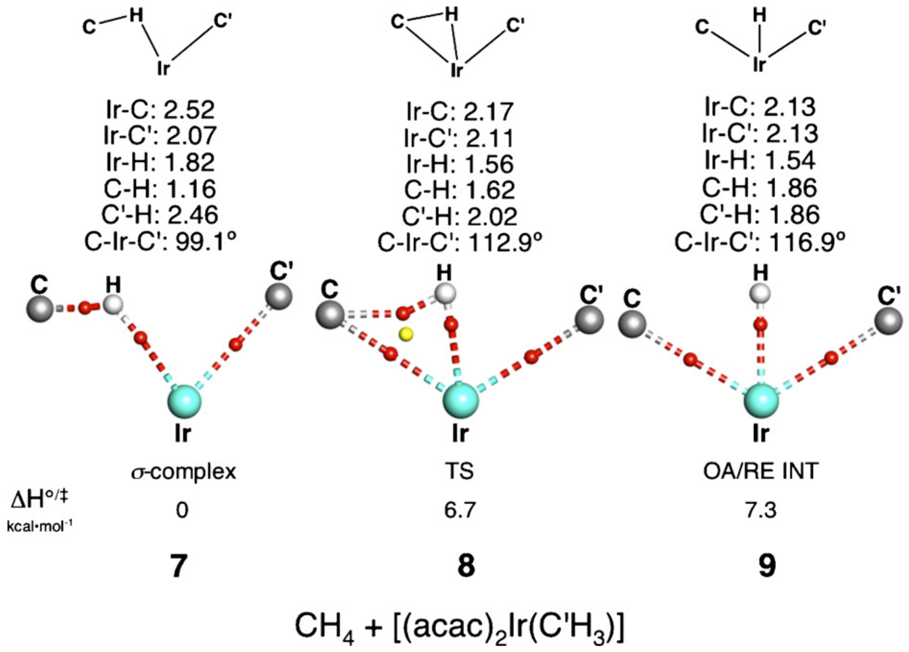

Fig. 3. Optimized geometric parameters and bonding patterns of **7**–**9**. The distances listed are in angstroms and the angles in degrees.

3.1.2. $CH_4 + [CpIrPH_3(C'H_3)]$

As anticipated for a σ-complex, the Ir–C and Ir–H distances in **4** are long. The calculated C–H bond distance is slightly longer than that of free methane, which indicates that the metal exhibits a small influence on this parameter. BCPs were found along the Ir–C′, Ir–H, and C–H coordinates. The σ-complex's interaction is manifested solely in the Ir–H bonding interaction, which is consistent with previously reported results for methane weakly coordinated to a metal [44].

In the TS for C–H bond cleavage (**5**), the C–H bond lengthens, the Ir–C and Ir–H distances shorten, and the Ir–C′ bond length lengthens slightly. The largest geometric change is in the Ir–C distance as it prepares to form the bond, while the second largest change is in the C–H bond as it prepares to break. The C–Ir–C′ angle is much wider in this TS than in the precursor σ-complex. Species **5** is characterized by the same bonding patterns as **4**; thus, the Ir–C and C–H bonds are formed and broken, respectively, after the TS is passed.

The geometric parameters of **6** are consistent with an Ir^V species. The Ir–C, Ir–C′, Ir–H distances of 2.18, 2.18, and 1.54 Å, respectively, are similar to those of other Ir–C and –H bonds, respectively, and the C–Ir–C′ is wide at ~128°. BCPs were found along the Ir–C and Ir–H coordinates and not along either C–H or H–C′, results consistent with expectations and with those previously reported for OA intermediates [15].

Relative to **4**, the enthalpic barrier for C–H bond cleavage ($\Delta H^{\ddagger}_{5-4}$) is 8.7 kcal mol^{-1}, and the formation of the intermediate (ΔH°_{6-4}) is slightly endothermic at 4.4 kcal mol^{-1}. The thermodynamic value for the formation of **6** agrees well with the value reported previously [4e], but the enthalpic barrier to C–H bond cleavage is lower by ~3 kcal mol^{-1} with the larger basis set used here.

3.1.3. $CH_4 + [(acac)_2Ir(C'H_3)]$

In **7**, methane is weakly bound to the iridium center through one σ-C–H bond. The calculated C–H bond length is again slightly longer than that of free methane, which would indicate a small effect from the metal on this geometric parameter. Compared to **4**, the analogous Ir–C and Ir–H distances are shorter by ~0.2 and ~0.1 Å, respectively. In the AIM analysis, **7** is characterized by Ir–C′, Ir–H, and C–H BCPs, and even with the shorter Ir–C distance, the methane to iridium bonding in the σ-complex is manifested solely through the Ir–H interaction.

Relative to the values in **7**, the Ir–C and Ir–H distances decrease by ~0.3 Å and the C–H distance increases by ~0.5 Å in forming the TS, **8**. A BCP is located along the Ir–C coordinate, which is consistent with the shorter length here compared to that in **5**. BCPs are also located along the Ir–C′, Ir–H, and C–H coordinates as they were in **5**. However, the formation of the Ir–C bond here creates a RCP inside the Ir–C–H coordinates. The activation of the C–H bond occurs later along the reaction coordinate in the bis-acac system, which is reflected in the shorter Ir–C and longer C–H distances and presence of Ir–C BCP in **8**.

For the intermediate, **9**, the bond distances, intra-ligand distances, and C–Ir–C angle are consistent with an Ir^V intermediate, and BCPs are located along the Ir–C and Ir–H coordinates.

Relative to **7**, the energies (E_e) of **8** and **9** are 8.5 and 8.1 kcal mol^{-1}, respectively. Thus, **9** is in a very shallow minimum, and the TS (**8**) is very late in the reaction path. Such a shallow minimum results in enthalpic differences of 6.7 and 7.3 kcal mol^{-1}. Examination of the zero-point energies at the harmonic level predicts that the intermediate here does not exist, but the harmonic approximation typically is not accurate for such a shallow minimum.

We have presented the bonding patterns that are characteristic of the σBM and OA/RE mechanism, and in the case of the later mechanism we have shown how these patterns change along the reaction coordinate and vary with differing "spectator" ligands. We now describe the bonding patterns that can be found in between these two classic cases.

3.2. Bonding patterns of representative models for mechanisms of alternative character

Previously, we concentrated on descriptions of the characteristic bonding patterns for the midpoint species along the σBM and OA/RE pathways [15]. For hydrogen transfer reactions in which

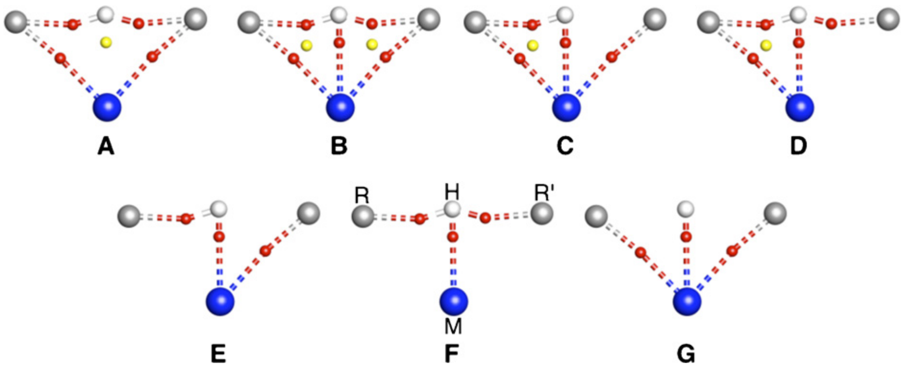

Fig. 4. All possible degrees of connectivity for a four-centered geometry. These patterns are for hydrogen transfer between R and R′ supported by a metal, M.

there is OA INT this midpoint represents that species, while for those reactions without an INT this midpoint corresponds to the TS. We also considered several representative models for alternative mechanisms and identified bonding patterns with differing degrees of connectivity [15]. Here, we consider all possible degrees of connectivity by presenting in general form the bonding patterns for metal (M) mediated hydrogen transfer between R and R′. These bonding patterns (**A** → **G**) are shown in Fig. 4.

The first bonding pattern, **A**, is characterized by M–R, M–R′, R–H, and R′–H BCPs with a RCP inside the coordinates of the four atoms; the metal supports only the pendent ligands and the hydrogen interacts only with the pendent ligands. Pattern **A** has already been identified with the TS for σBM. As the M–H interaction strengthens, a BCP should appear along the M–H coordinate, which creates two RCPs inside the M–R–H and M–R′–H coordinates; together these form the characteristic pattern in **B**. In this pattern, which has the highest possible degree of connectivity, the metal supports the pendent ligands and the transferring hydrogen.

We can rationalize the next two bonding patterns (**C**, **D**) by considering the coalescence of one BCP with one RCP of **B**. Bader described the points in the density where a BCP and RCP coalesce and annihilate as the "catastrophe point of the conflict type" [14]. For example, if the R′–H BCP coalesces with its corresponding RCP, they annihilate and produce pattern **C**. Instead, if the M–R′ BCP coalesces with its corresponding RCP, they annihilate and produce pattern **D**. In **C**, the metal again supports the pendent ligands and the transferring hydrogen, but the interaction between the transferring hydrogen and one pendent ligand is lost, a pattern already identified in the TS for OA in $[(acac)_2Ir(CH_3)(C'H_3)H]^{\ddagger}$. However, in **D**, the metal supports only one pendent ligand and the transferring hydrogen while the interactions between the pendent ligands and the transferring hydrogen are retained.

The remaining three sets of bonding patterns can be rationalized by the coalescence of both RCPs with BCPs from **B**. Coalescence of the M–R–H and M–R′–H RCPs with the M–R and R′–H BCPs results in pattern **E** where the metal interacts with only one pendent ligand (excluding the transferring hydrogen) and the transferring hydrogen interacts with only one pendent ligand, a pattern seen in the TS for OA in $[[CpIrPH_3(CH_3)(C'H_3)H]^+]^{\ddagger}$. Next, the coalescence of the M–R–H and M–R′–H RCPs with the respective M–R and –R′ BCPs results in pattern **F**. Here, the metal supports only the transferring hydrogen, which retains R–H and R′–H interactions. Lastly, the coalescence of the M–R–H and M–R′–H RCPs with the R–H and R′–H BCPs results in **G**, which is the typical pattern for the OA/RE intermediate, where the metal interacts with only the pendent ligands, consistent with our understanding of the bonding in these intermediates.

Somewhat to our surprise, we found all the remaining possible patterns (**A** → **G**), when we analyzed the bonding of the midpoint species of three reaction types for a variety of metals and charges: (**Rxn1**) $C_6H_6 + [(acac)_2M(CH_2CH_2Ph)]$ (M = Fe$^-$ (**10**), Co (**11**), Ni$^+$ (**12**), Ru$^-$ (**13**), Rh (**14**), Pd$^+$ (**15**), Os$^-$ (**16**), Ir (**17**), Pt$^+$ (**18**)), (**Rxn2**) $C_6H_6 + [TpM(CO)(CH_2CH_2Ph)]$ (M = Mn$^-$ (**19**), Fe (**20**), Co$^+$ (**21**), Tc$^-$ (**22**), Ru (**23**), Rh$^+$ (**24**), Re$^-$ (**25**), Os (**26**), Ir$^+$ (**27**)), and (**Rxn3**) $CH_4 + [CpM(CO)(B(OCH_2)_2)]$ (M = Mn$^-$ (**28**), Fe (**29**), Co$^+$ (**30**), Tc$^-$ (**31**), Ru (**32**), Rh$^+$ (**33**), Re$^-$ (**34**), Os (**35**), Ir$^+$ (**36**)). The geometries, bonding patterns, and relative energies are described in their respective section. Those systems that proceed by a σBM-like pathway where one TS connects reactant and product are labeled "Pathway 1" and the energy barrier in this pathway is that between the reactant and the TS for hydrogen transfer. Those systems that proceed by the OA/RE pathway are labeled "Pathway 2" and the energy barrier in this pathway is that between the reactant and the TS that results in the OA intermediate. For the first two reactions, the carbon atoms of the phenyl and ethylbenzene ligands are labeled C^{sp2} and C^{sp3}, respectively.

Table 2
Relative energies (kcal mol^{-1}) for $C_6H_6 + [(acac)_2M(CH_2CH_2Ph)]$ (**Rxn1**)

Metal	Pathway	Reac → TS				Reac → (Prod, INT)			
		$\Delta E_0^{\ddagger}$	$\Delta E^{\ddagger}$	$\Delta H^{\ddagger}$	$\Delta G^{\ddagger}$	ΔE_0	ΔE°	ΔH°	ΔG°
Fe$^-$ (**10**)	1[a]	7.91	8.46	7.87	21.08	−5.90	−5.86	−5.86	−5.51
Co (**11**)	1[a]	16.27	16.74	16.15	30.02	−1.31	0.12	−0.47	9.05
Ni$^+$ (**12**)	1[a]	37.40	38.06	37.47	50.39	28.75	30.25	29.66	38.08
Ru$^-$ (**13**)	1	3.89	3.69	3.69	4.69	−8.01	−7.82	−7.82	−8.01
Rh (**14**)	1	13.93	13.62	13.62	14.67	−3.43	−3.35	−3.35	−3.51
Pd$^+$ (**15**)	1	21.03	20.65	20.65	21.94	8.28	8.50	8.50	6.53
Os$^-$ (**16**)	2	NF	NF	NF	NF	−26.47	−25.86	−26.46	−12.80
Ir (**17**)	1	5.47	5.37	5.37	5.04	−3.33	−3.22	−3.22	−3.58
Pt$^+$ (**18**)	1	19.01	18.77	18.77	19.44	5.74	5.89	5.89	5.29

[a] Energies relative to $C_6H_6 + [(acac)_2M(CH_2CH_2Ph)]$.

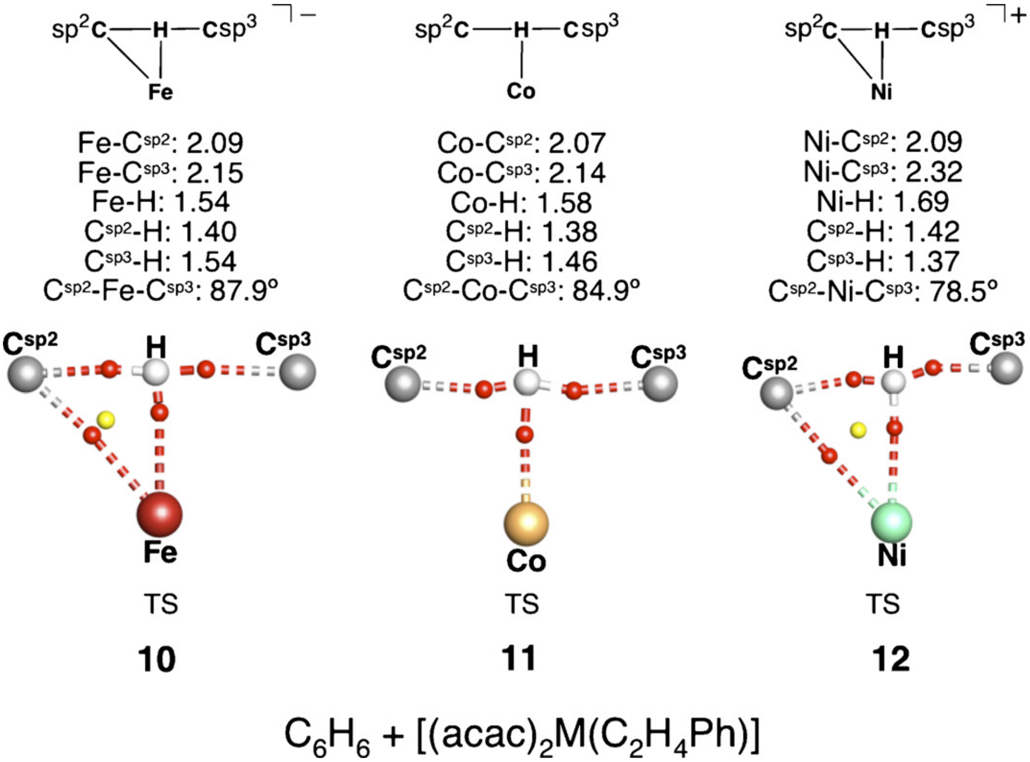

Fig. 5. Optimized geometric parameters and bonding patterns of **10**–**12**. The distances listed are in angstroms and the angles in degrees. By assigning the cc-pVDZ basis set to cobalt in **11**, the Co–C^{sp2} BCP and corresponding RCP were located.

3.2.1. *Rxn1, C_6H_6 + [(acac)$_2$M(CH_2CH_2Ph)]*

The relative energies (kcal mol^{-1}) for the first, second, and third row analogs of this reaction for the anionic, neutral, or cationic species are reported in Table 2. Unless noted otherwise, the reactants are the σ-bound benzene complexes, [(acac)$_2$M(σ-C_6H_6)(CH_2CH_2Ph)], and the energies are relative to these species. In Table 2, the "products" are either the σ-bound ethylbenzene complexes, [(acac)$_2$M(C_6H_5)(σ-CH_3CH_2Ph)] (Pathway 1), or the OA intermediates, [(acac)$_2$M(CH_2CH_2Ph)(C_6H_5)H] (Pathway 2).

The optimized geometric parameters and bonding patterns for Fe$^-$ (**10**), Co (**11**), and Ni$^+$ (**12**) series are shown in Fig. 5. Geometrically, the M–C^{sp2} and C^{sp2}–H bonds appear similar in the three species. The M–C^{sp3} distance increases by ~0.15 Å in **12** compared to similar values in **10** and **11**. The M–H distances increase, and the C^{sp3}–H distances and C^{sp3}–M–C^{sp2} angles decrease in value along the series. Species **10** and **12** are characterized by the same bonding pattern: M–C^{sp2}, M–H, C^{sp3}–H and C^{sp2}–H BCPs are located along these respective coordinates, and a RCP is located inside each M–C^{sp2}–H triangle. However, **11** is characterized by Co–H, C^{sp3}–H, and C^{sp2}–H BCPs but is missing the M–C^{sp2} BCP in spite having the shortest M–C^{sp2} distance. To check this apparent anomaly, cobalt was assigned the all-electron cc-pVDZ basis set and a Co–C^{sp2} BCP and the corresponding Co–C^{sp2}–H RCP were now located.

For all three of these systems, the reactants are taken as free benzene and [(acac)$_2$M(CH_2CH_2Ph)] because the corresponding [(acac)$_2$M(σ-C_6H_6)(CH_2CH_2Ph)] complexes were not located. The barriers to hydrogen transfer increase along this series as the metal is replaced, paralleled by the trend in reaction energies, which increase in energy and switch from exothermic and exergonic to endothermic and endergonic.

For Ru$^-$ (**13**), Rh (**14**), and Pd$^+$ (**15**), the M–C^{sp2}, M–C^{sp3}, and M–H distances increase while the C^{sp3}–H, C^{sp2}–H, and C^{sp3}–M–C^{sp2} parameters decrease along this series (Fig. 6). In the bonding analysis, **13** is characterized by Ru–C^{sp2}, Ru–C^{sp3}, Ru–H, and C^{sp3}–H BCPs with a RCP inside the Ru–C^{sp3}–H coordinates. In **14**, the M–C^{sp3} BCP disappears and a C^{sp2}–H BCP appears, which parallels the lengthening and shortening of the respective distances. A RCP is also found in this species but inside the Rh–H–C^{sp2} coordinates. Species **15** is characterized by full connectivity as Pd–C^{sp2}, Pd–C^{sp3}, Pd–H, C^{sp2}–H, and C^{sp3}–H BCPs are located; and RCPs are located inside the Pd–C^{sp2}–H and Pd–C^{sp3}–H coordinates, respectively. The geometric coordinates and bonding patterns of these species are shown in Fig. 6. Although these three related systems appear quite different, the RCPs are quite close to the BCPs and they will annihilate each other when combined. Thus, the patterns in **13** and **14**, although different can both be generated from the pattern in **15**.

The barrier for hydrogen transfer is small (3.7 kcal mol^{-1}) in the ruthenium system, and the formation of the σ-bound ethylbenzene complex is exothermic by 7.8 kcal mol^{-1}. The barrier is greater by ~10 kcal mol^{-1} in the rhodium system, but the overall reaction is still exothermic and exergonic at 3.4 and 3.5 kcal mol^{-1}, respectively. The enthalpic and free energy barriers are higher in the palladium system (20.7 and 21.9 kcal mol^{-1}), and product formation is now endothermic and endergonic by 8.5 and 6.5 kcal mol^{-1}, respectively.

For the third row models, Os$^-$ (**16**), Ir (**17**), and Pt$^+$ (**18**), the M–C^{sp2} distances are once again similar between the three systems, and the M–C^{sp3} distances are the only coordinates that lengthen as the metal is replaced. The M–H distances oscillate while the C^{sp2}–H and C^{sp3}–H distances and C^{sp2}–M–C^{sp3} angles decrease as the metal is replaced. In the bonding analysis, **16** is characterized by metal–ligand BCPs as anticipated for an intermediate. For **17**, BCPs are located along the Ir–C^{sp2}, Ir–C^{sp3}, Ir–H, and C^{sp3}–H coordinates; a RCP is found inside the Ir–C^{sp3}–H coordinates. Like the palladium congener, **18** is characterized by full connectivity; BCPs are

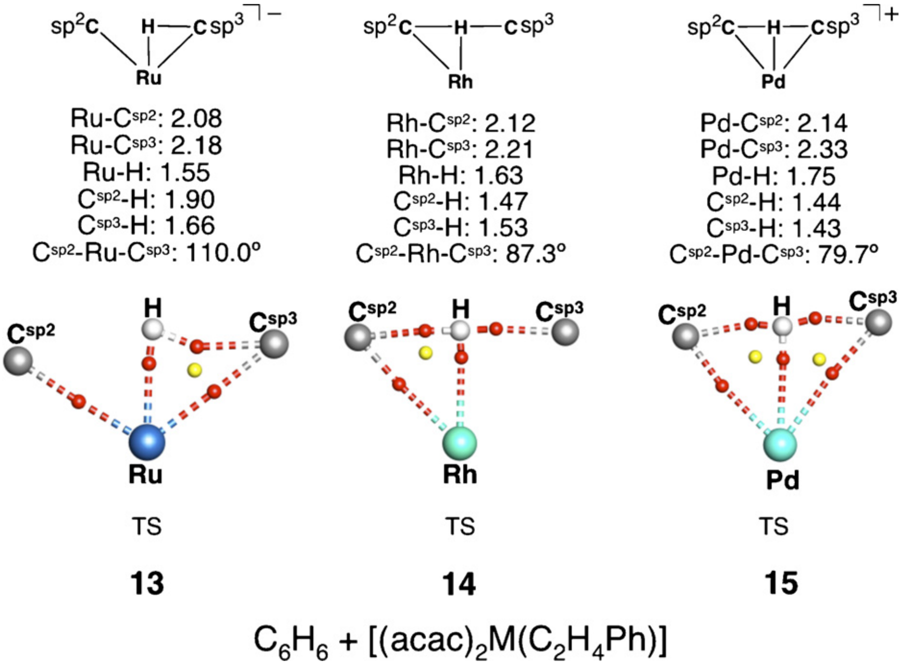

Fig. 6. Optimized geometric parameters and bonding patterns of **13**–**15**. The distances listed are in angstroms and the angles in degrees. The larger all-electron basis set, TZVPP, was assigned to the rhodium in **14** and a Rh–C^{sp3} BCP was not located even at with this basis set.

located along the Pt–C^{sp2}, Pt–C^{sp3}, Pt–H, C^{sp2}–H, and C^{sp3}–H coordinates, and RCPs are located inside the Pt–C^{sp2}–H and Pt–C^{sp3}–H coordinates, respectively. These results are shown in Fig. 7.

Similar trends in the relative energies are calculated for the third row analogs. Product formation becomes more endothermic and endergonic as the metal is replaced. In the osmium system, the formation of the OA INT, **16**, is more exothermic than the iridium and platinum systems; however, the Os system proceeds through Pathway 2. The enthalpic and free energy barriers in the iridium system are small at 5.4 and 5.0 kcal mol^{-1}, respectively, and the overall reaction is exothermic and exergonic by 3.2 and 3.6 kcal mol^{-1}, respectively. Like the palladium system, the barrier for hydrogen transfer is large in the platinum system (18.8 kcal mol^{-1}), and the product formation is endothermic (5.9 kcal mol^{-1}).

In descending down the group 8 metals, the M–C^{sp3} bond is formed and the C^{sp2}–H bond is broken between **10** and **13**. The C^{sp3}–H is then broken between **13** and **16**. For group 9, the M–C^{sp3} bond is formed in the iridium species, but the bond is not broken. Likewise, for group 10, the M–C^{sp3} bond is formed in the palladium and platinum congeners. As the metal is replaced down each period, the barriers decrease in energy and product formation also decreases in energy.

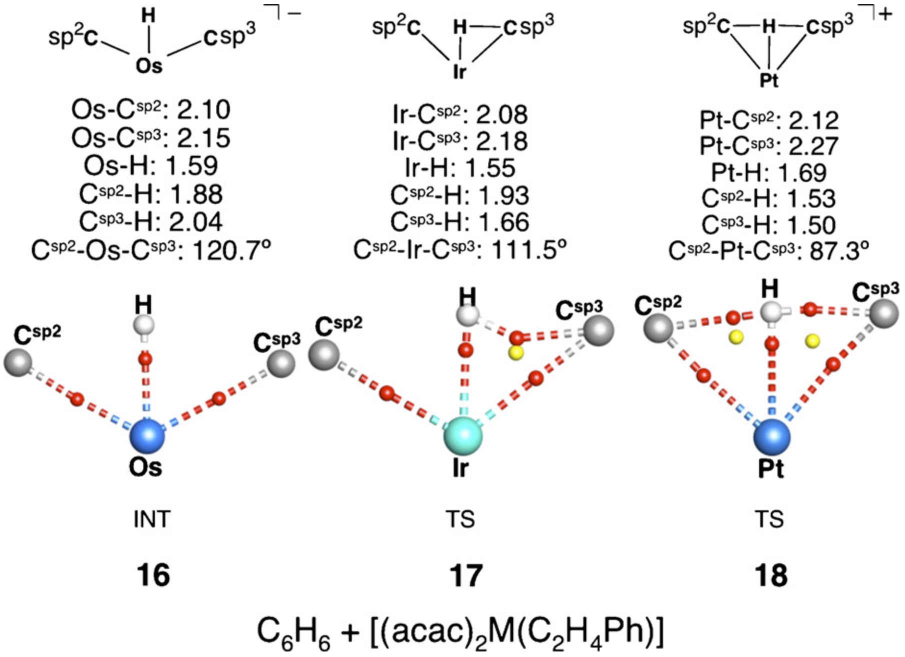

Fig. 7. Optimized geometric parameters and bonding patterns of **16**–**18**. The distances listed are in angstroms and the angles in degrees.

Table 3
Relative energies (kcal mol^{-1}) for C_6H_6 + [TpM(CO)(CH_2CH_2Ph)] (**Rxn2**)

Metal	Pathway	Reac → TS				Reac → (Prod, INT)			
		$\Delta E_0^\ddagger$	$\Delta E^\ddagger$	$\Delta H^\ddagger$	$\Delta G^\ddagger$	ΔE_0	ΔE°	ΔH°	ΔG°
Mn^-	1	8.26	7.77	7.77	9.80	−10.21	−9.88	−9.88	−11.07
Fe	1	14.71	14.45	14.45	16.82	−6.26	−5.72	−5.72	−6.74
Co^+	1	14.76	14.26	14.26	16.03	−0.89	−0.77	−0.77	−1.42
Tc^-	2	NF	NF	NF	NF	−0.12	−0.10	−0.10	−0.37
Ru	1	11.71	11.42	11.42	12.53	−7.14	−6.97	−6.97	−7.98
Rh^+	1	18.74	18.36	18.36	19.64	−0.17	−0.06	−0.06	−0.70
Re^-	2[a]	NF	NF	NF	NF	NF	NF	NF	NF
Os	2	0.51	0.20	0.20	0.93	0.58	0.52	0.52	0.79
Ir^+	1	12.92	12.69	12.69	13.73	−3.69	−3.59	−3.59	−3.91

[a] Reactant $[TpRe(CO)(\sigma\text{-}C_6H_6)(CH_2CH_2Ph)]^-$ was not located.

3.2.2. *Rxn2, C_6H_6 + [TpM(CO)(CH_2CH_2Ph)]*

For this reaction similar analyses were performed for the first TM row (Mn^- (**19**), Fe (**20**), Co^+ (**21**)); second TM row (Tc^- (**22**), Ru (**23**), Rh^+ (**24**)); and third TM row (Re^- (**25**), Os (**26**), Ir^+ (**27**)) metals. The relative energies (kcal mol^{-1}) for the first, second, and third row analogs for this system are reported in Table 3. The reactants, TSs, and products for these systems are defined the same way as in the previous system.

In this series of first row species: the M–C^{sp2} and C^{sp2}–M–C^{sp3} parameters oscillate, the M–C^{sp3} and C^{sp2}–H distances decrease from their values in **19** to identical distances in **20** and **21**, respectively, and the M–H distance increases and the C^{sp3}–H distances decrease. In the bonding analysis, **19** is characterized by Mn–C^{sp3}, Mn–H, C^{sp2}–H, and C^{sp3}–H BCPs with a RCP located inside the Mn–C^{sp3}–H coordinates. Species **20** and **21** are characterized by the same bonding patterns; only M–H, C^{sp2}–H, and C^{sp3}–H BCPs were located. The results of these analyses for these species are presented in Fig. 8. One should note that the RCP and one BCP are quite close in **19**; their coalescence will produce the same pattern as that found for **20** and **21**.

Once again, the energy barrier to hydrogen transfer increases along this series; however, the values of the iron and cobalt systems are similar. The product is more exothermic in the manganese system and becomes isenthalpic with the reactant in the cobalt system.

For the second transition row systems, **22**, **23**, and **24**, the M–C^{sp3} and M–H distances oscillate, the C^{sp3}–H, C^{sp2}–H distances and C^{sp3}–M–C^{sp2} angles decrease, and the M–C^{sp3} distances increase along this series. In the bonding analysis, BCPs are only found along the Tc–C^{sp3}, Tc–C^{sp2}, and Tc–H coordinates in **22**, characteristics expected of an intermediate. Species **23** is characterized by full connectivity; Ru–C^{sp2}, Ru–C^{sp3}, Ru–H, C^{sp2}–H, and C^{sp3}–H BCPs were found along these coordinates as expected for the >20° decrease in the C^{sp2}–M–C^{sp3} angle. RCPs were found inside the Ru–C^{sp2}–H and Ru–C^{sp3}–H coordinates, respectively. As the Rh–C^{sp3} distance increases in **22** the Rh–C^{sp3} BCP and the Rh–C^{sp3}–H RCP are lost, but the other BCPs are retained. The optimized geometric parameters and bonding patterns of these species are shown in Fig. 9.

The general increase in energy of the barrier is not seen for the second row analogs as the technetium system proceeds by a different pathway than the ruthenium and rhodium systems. For the technetium system, the OA intermediate (**22**) is isenthalpic with the reactant, but all attempts to locate the TS for oxidative C–H bond cleavage failed. For the ruthenium and rhodium systems, the energy barrier increases from one metal to the next and product formation becomes less exothermic.

In the third transition row systems, **25**, **26**, and **27**, the M–C^{sp2} distance decreases by 0.03 Å from the value in **25** to identical values in **26** and **27**. The M–C^{sp3} and M–H distances oscillate between the three species, while the C^{sp2}–H distance, the C^{sp3}–H distance, and the C^{sp2}–M–C^{sp3} angle, decrease along this series. In the bonding analyses of these species, M–C^{sp2}, M–C^{sp3}, and M–H BCPs are located in **25** and **26**, which are both intermediates. Species **27** is characterized by full connectivity; BCPs were located along the Ir–C^{sp2}, Ir–C^{sp3}, Ir–H, C^{sp2}–H, and C^{sp3}–H coordinates, and RCPs are located inside the Ir–C^{sp3}–H and Ir–C^{sp2}–H coordinates, respectively; note that **27** is close to having a pattern like **25** and **26**. The results for these complexes are shown in Fig. 10.

The σ-bound benzene reactant and the TS for oxidative C–H bond cleavage were not located in the rhenium system; all attempts to optimize these species resulted in the oxidized intermediate, which is significantly more stable than the reactant. For osmium, the barriers to oxidative C–H bond cleavage appear lower in energy than product formation. The relative SCF energies for the TS and product are 1.8 and 1.0 kcal mol^{-1}, respectively, but zero-point corrections produce lower thermally corrected barriers. The barrier to hydrogen transfer is moderate in the iridium system at 12.7 kcal mol^{-1}, and product formation is exothermic by 3.6 kcal mol^{-1}.

For the group 7 metals, the C^{sp2}–H and C^{sp3}–H bonds are broken and the M–C^{sp2} bond is formed in switching between manganese and technetium. For group 8, the M–C^{sp2} and M–C^{sp3} bonds are formed in the ruthenium species prior to breaking the C^{sp2}–H and C^{sp3}–H bonds in the osmium species. Lastly, for group 9, the M–C^{sp2} bond is formed in the rhodium species prior to forming the M–C^{sp3} bond in the iridium species.

3.2.3. *Rxn3, CH_4 to [CpM(CO)($B(OCH_2)_2$)]*

The relative energies for these systems are presented in Table 4. All of these systems proceed by Pathway 1; the reactants and products are the σ-bound methane and σ-bound borane complexes, respectively.

The optimized geometric parameters and bonding patterns of the first TM row species, Mn^- (**28**), Fe (**29**), and Co^+ (**30**), are shown in Fig. 11. Along this series, the M–B distance is identical in **28** and **29**, but lengthens slightly in **30**, while the M–H distance decreases from **28** to an identical value in **29** and **30**. The M–C, B–H, and B–M–C parameters decrease along this series; only the C–H distance lengthens in this series. In the bonding analysis, BCPs are found along the Mn–B, Mn–H, and C–H coordinates in **28**. The analogous BCPs are located in **29** along with a B–H BCP and a RCP inside the M–B–H coordinates; however, the B–H BCP coalesces with the RCP and annihilates the BCP at the double-ζ level in the basis for iron. In **30**, the M–B BCP is lost, which parallels the lengthening of this bond; only M–H, C–H, and B–H BCPs were located.

The results of similar analyses of the second row analogs (Tc^- (**31**), Ru (**32**), Rh^+ (**33**)) are shown in Fig. 12. In these species, the M–B and B–M–C parameters oscillate; the M–C, M–H and B–H

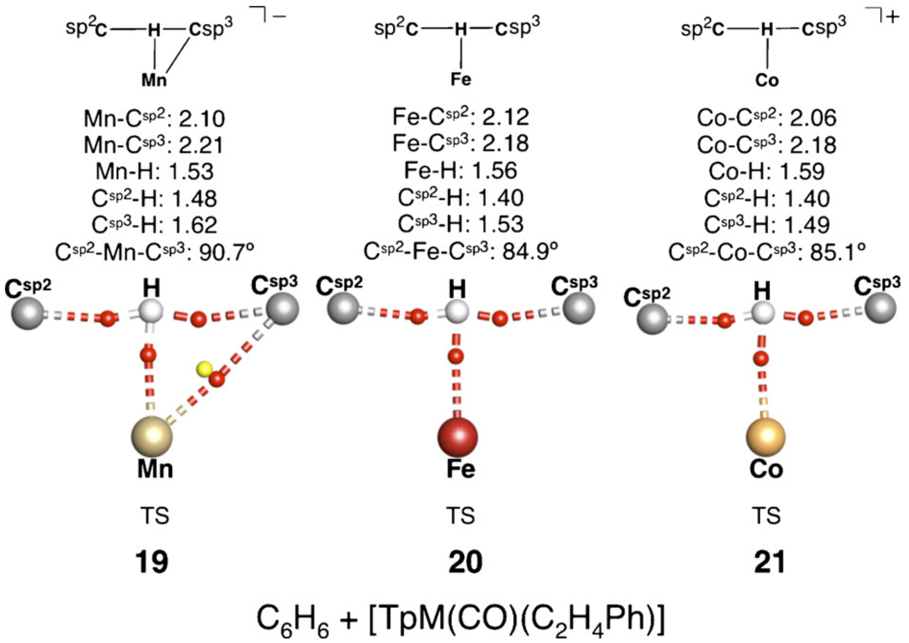

Fig. 8. Optimized geometric parameters and bonding patterns of **19**–**21**. The distances listed are in angstroms and the angles in degrees.

distances decrease; and the C–H distance increases in this series. Species **31** and **32** exhibit the same bonding patterns; M–B, M–H, and C–H BCPs were located in these species. A M–C BCP forms along this coordinate in **33**, which is also exhibits the shortest M–C distance.

The third row analogs (Re$^-$ (**34**), Os (**35**), Ir$^+$ (**36**)—Fig. 13) exhibit the same geometric trends for the first five parameters listed as the second row analogs. The C–M–B angles, however, increase in this series rather than oscillate. These species exhibit the same bonding patterns as their second row analogs.

The rhenium and osmium systems exhibit negative enthalpic barriers. The $\Delta E^{\ddagger}_{\mathrm{SCF}}$ values are, of course, positive for these two systems (0.6 and 1.8 kcal mol^{-1}, respectively). Again the very low electronic energy barriers are overwhelmed by the harmonic vibrational corrections. The formation of the σ-bound borane products are exothermic by 24.1 and 13.4 kcal mol^{-1} for the rhenium and osmium systems, respectively. For the iridium system, the enthalpic and free energy barriers are small at 4.7 and 6.7 kcal mol^{-1}, respectively, and the formation of the σ-bound borane complex is exothermic by 1.2 kcal mol^{-1} but is slightly endergonic by 0.9 kcal mol^{-1}.

The iridium system is characterized by similar energies to those of the iron system, which is the experimental system. The barriers to hydrogen transfer are smaller in the former, and product formation

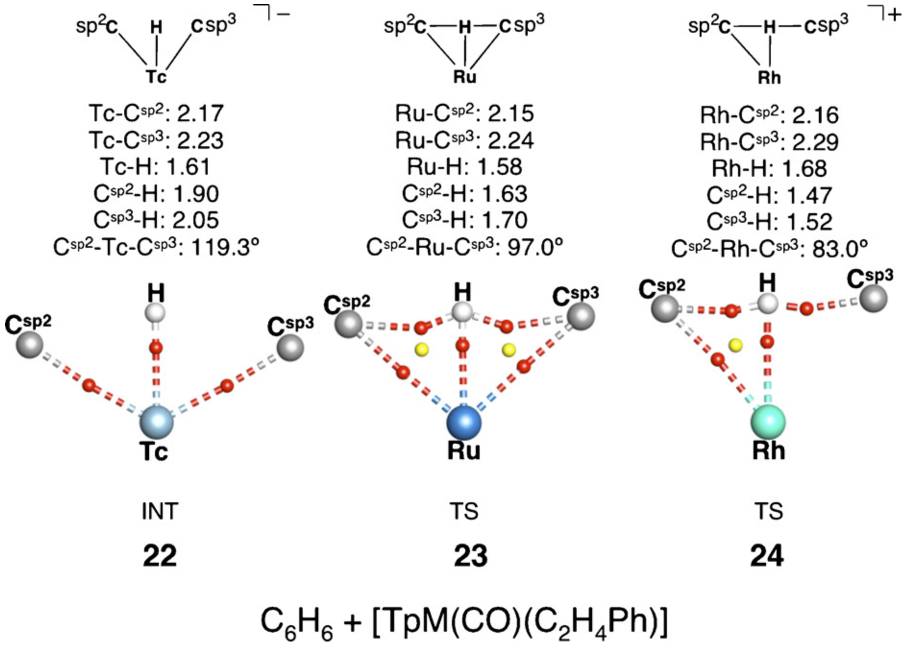

Fig. 9. Optimized geometric parameters and bonding patterns of **22**–**24**. The distances listed are in angstroms and the angles in degrees.

Table 4
Relative energies (kcal mol^{-1}) for CH_4 + [CpM(CO)(B(OCH$_2$)$_2$)] (**Rxn3**)

Metal	Pathway	Reac → TS				Reac → Prod			
		$\Delta E_0^{\ddagger}$	$\Delta E^{\ddagger}$	$\Delta H^{\ddagger}$	$\Delta G^{\ddagger}$	ΔE_0	ΔE°	ΔH°	ΔG°
Mn$^-$	1	4.18	3.30	3.30	5.97	−8.79	−9.85	−9.85	−6.38
Fe	1	8.23	7.48	7.48	9.58	1.04	0.28	0.28	2.66
Co$^+$	1	13.17	12.38	12.38	14.56	6.42	5.77	5.77	7.47
Tc$^-$	1	2.10	1.39	1.39	3.41	−14.16	−15.09	−15.09	−12.14
Ru	1	7.11	6.40	6.40	8.44	−0.97	−1.75	−1.75	0.57
Rh$^+$	1	15.03	14.47	14.47	17.14	8.34	7.59	7.59	9.84
Re$^-$	1	−0.56	−1.17	−1.17	0.37	−23.30	−24.07	−24.07	−21.67
Os	1	0.45	−0.08	−0.08	1.44	−12.65	−13.42	−13.42	−10.64
Ir$^+$	1	5.37	4.74	4.74	6.65	−0.55	−1.23	−1.23	0.92

is slightly exothermic. It remains to be seen if the iridium system can accomplish this chemistry.

3.2.4. *Effects of spectator ligand on bonding patterns*

The effect of spectator ligand on the bonding patterns were considered by studying the reaction: CH_4 + [LM(PH$_3$)H′] (M = Fe, Ru, Os). The ligands (L) considered for this study are Cp, Tp, a tris–carbene ligand [45] (HB(NHC)$_3$) that is similar to Tp, and a tris–phosphine ligand [46] (HB(PMe$_2$CH$_2$)$_3$ = HBP$_3$). The results for [LFe(PH$_3$)(CH$_3$)(H)(H′)] (L = Cp (**37**), Tp (**37a**), HB(NHC)$_3$ (**37b**), HBP$_3$ (**37c**)) are presented in Fig. 14. The results for the ruthenium analogs, [LRu(PH$_3$)(CH$_3$)(H)(H′)] (L = Cp (**38**), Tp (**38a**), HB(NHC)$_3$ (**38b**), HBP$_3$ (**38c**)), are presented in Fig. 15. Likewise, the results for the osmium analogs, [LOs(PH$_3$)(CH$_3$)(H)(H′)] (L = Cp (**39**), Tp (**39a**), HB(NHC)$_3$ (**39b**), HBP$_3$ (**39c**)) are shown in Fig. 16.

In the geometric analyses of the iron species, the Fe–C, Fe–H, distance lengthens and the C–Fe–H′ angle decreases along this series. The Fe–H′, C–H, and H–H′ distances oscillate between the species. In the bonding analysis, **37** is characterized by Fe–H, Fe–H′, C–H, and H–H′ BCPs; a RCP is found inside the Fe–H–H′ coordinates. However, the H–H′ and Fe–H–H′ RCP coalesce and the BCP is lost along the Fe–H′ coordinate in **37a**. Species **37b** and **37c** exhibit the same bonding patterns as the Tp analog. The loss of the BCP along the Fe–H′ coordinate parallels the increasing bond distance from **37** to **37c**.

In the geometric analyses of the ruthenium analogs, the Ru–C and Ru–H′ distances lengthen, the Ru–H and C–H distances oscillate, and the H–H′ and C–Ru–H parameters decrease along this series. Interestingly, the ruthenium Cp analog, **38** is an intermediate with the expected patterns of BCPs. Species **38a** is characterized by Ru–C, Ru–H, Ru–H′ BCPs, and a RCP is found inside the Ru–C–H coordinates. The Ru–C BCP and RCP of **38a** coalesce and the BCP along the Ru–C coordinate is lost in **38b**. Despite having a longer Ru–C bond than in **38b**, a BCP is located along this coordinate in **38c**. Species **38c** is characterized by full connectivity as Ru–C, –H, –H′, C–H, and H–H′ BCPs were found along with RCPs inside the Ru–C–H and Ru–H–H′ coordinates. The strengthening of the C–H and H–H′ bonds in **38c** allows for Ru–C and Ru–H′ BCPs to be located even though these distances are the longest in the series.

In the osmium analogs, all of the geometric parameters oscillate as the ligand is replaced. Each species is an intermediate, and only Os–C, Os–H, and Os–H′ BCPs are located for these species. The character of the midpoint species, geometric parameters, and bonding patterns are insensitive to the change in ligand for this transition metal.

The influence of the spectator ligand on the bonding patterns is limited with both all iron and osmium species being insensitive. However, the four ruthenium species exhibit different bonding patterns. Consistent with an intermediate, **38** is characterized by only metal–ligand BCPs; however, **38c** exhibits full connectivity.

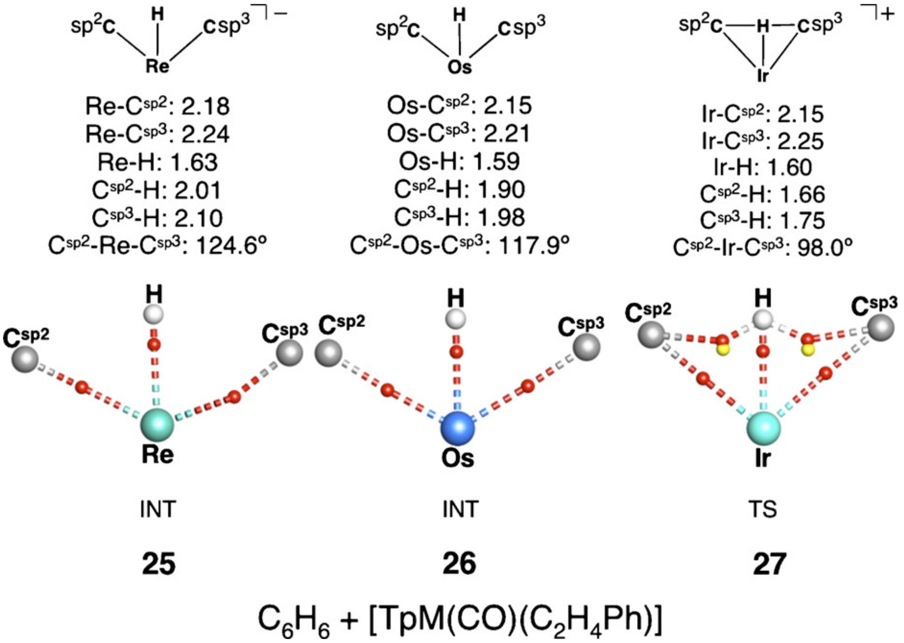

Fig. 10. Optimized geometric parameters and bonding patterns of **25**–**27**. The distances listed are in angstroms and the angles in degrees.

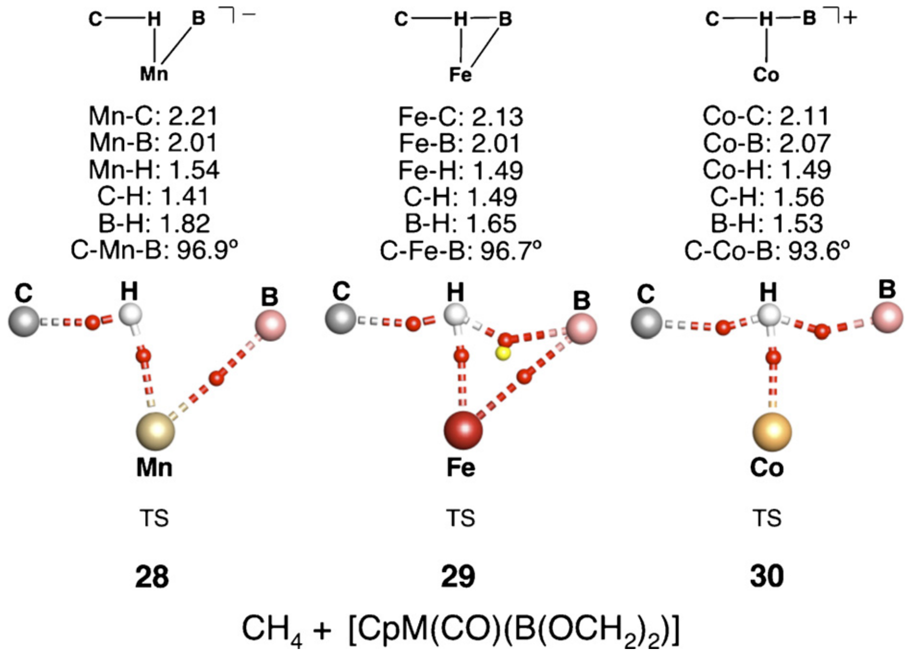

Fig. 11. Optimized geometric parameters and bonding patterns of **28**–**30**. The distances listed are in angstroms and the angles in degrees.

The degrees of connectivity of **38a** and **38b** are in between the Cp and HBP_3 analogs.

3.3. *Stability of bonding patterns*

To verify the stability of these bonding patterns, we examined seven models that correspond to one of the bonding patterns by assigning a higher-level basis set to the metal. The basis sets that were assigned to the non-metal atoms in the previous Bader's analyses were unchanged. Patterns **A**, **D**, **E**, and **F** were verified up to the quadruple-ζ level by assigning the cc-pVQZ basis set to the scandium, nickel, manganese, and iron centers of **1**, **12**, **28**, and **37a**, respectively. Patterns **B**, **C**, and **G** were verified at the triple-ζ level by assigning the TZVPP basis set to the palladium, ruthenium, and technetium centers of **15**, **38a**, and **22**, respectively. Thus, all seven patterns have been identified and verified at higher levels in the basis.

3.3.1. *Detailed analysis of basis set and density functional effects*

Here, we investigate in more detail the basis set and density functional (DF) effects on the CPs of **1**, where a single previously optimized geometry was used. A variety of basis sets and

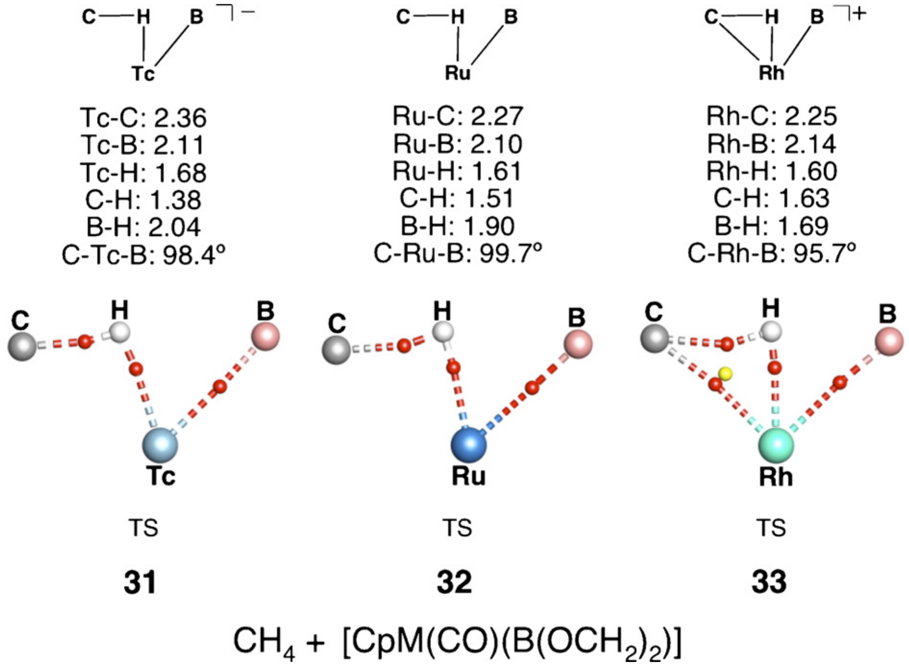

Fig. 12. Optimized geometric parameters and bonding patterns of **31**–**33**. The distances are reported in angstroms and angles in degrees.

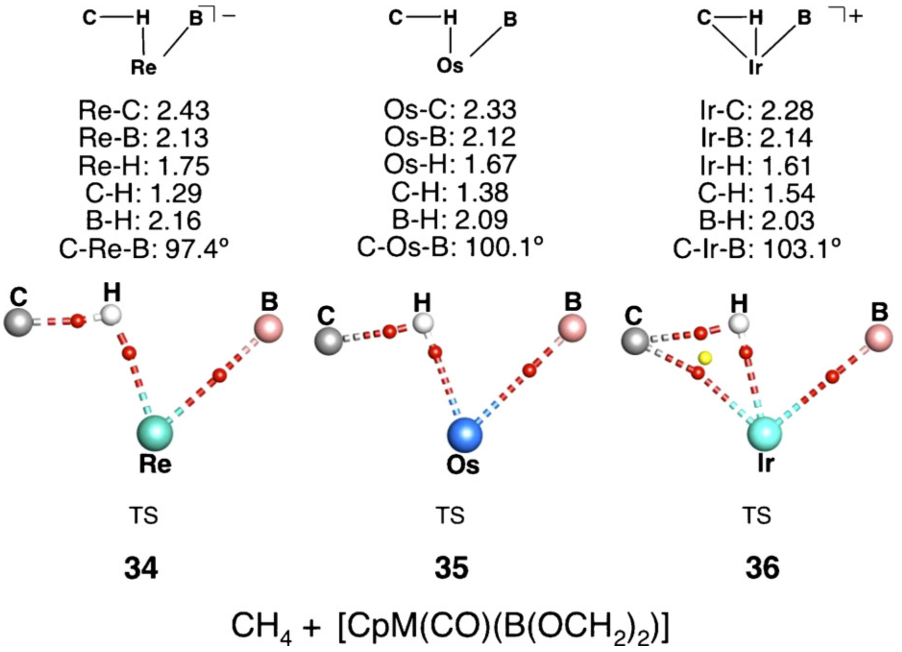

Fig. 13. Optimized geometric parameters and bonding patterns of **34**–**36**. The distances are reported in angstroms and angles in degrees.

DFs were considered in this analysis. Finally, **1** was individually optimized with four different basis sets assigned to scandium (the basis sets for the carbon and hydrogen atoms of section 1 remained the same) and the gradient fields were analyzed and compared.

3.3.2. *Basis sets*

For this investigation, the B3LYP/DZP coordinates of **1** and the B3LYP DF were used. The basis sets assigned to the carbon and hydrogen atoms in the previous analysis remain the same. The basis sets assigned to the scandium with the corresponding density and metric values for the Sc–C (**B**), C–H (**B**′), and ring (**R**) CPs of **1** are listed in Table 5. In Fig. 17, the CPs and atoms designations are defined and will be used throughout this section.

The values of the density at **B** calculated with the fully contracted basis sets are slightly smaller than those calculated with the split-valence, double-ζ, triple-ζ, and quadruple-ζ basis sets. The values of **B** and **B**′ increase to ∼0.052 and ∼0.128 (e/bohr^3), respectively, with the change in basis sets. The density value of **R** also increases slightly. Geometrically, the distances between the **B** and **R** to scandium are insensitive to the basis set. Likewise, the distance between the **B** and **R** remains ∼0.6 Å. For the Sc–**B**–C angles, a value of ∼168° is reported for all but the STO-*n*G (*n* = 3, 6) basis sets, which return a value smaller by ∼5°.

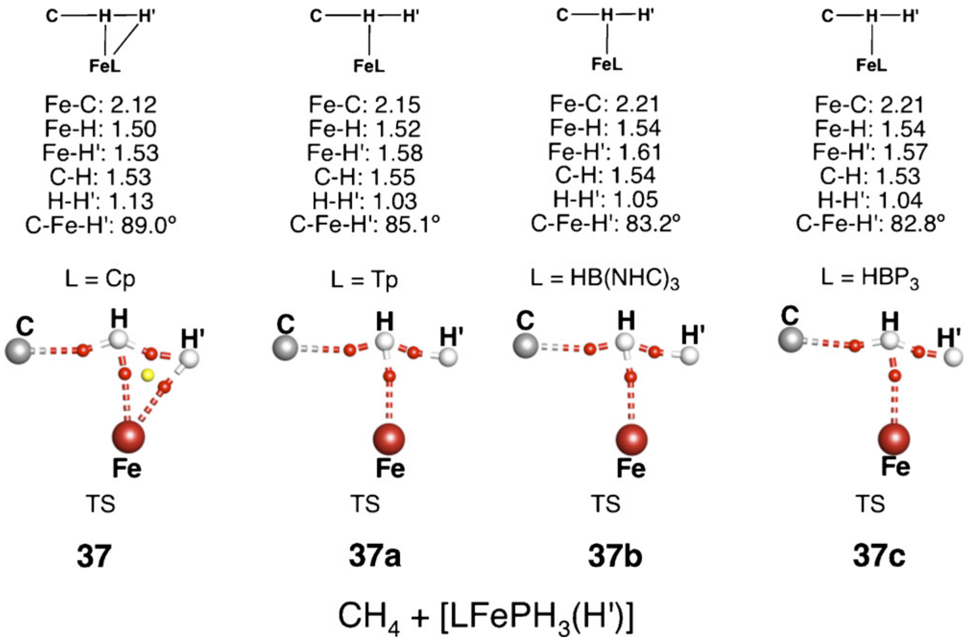

Fig. 14. Optimized geometric parameters and bonding patterns for **37** (L = Cp), **37a** (L = Tp), **37b** (L = HB(NHC)$_3$), and **37c** (L = HBP$_3$). The distances listed are in angstroms and the angles in degrees.

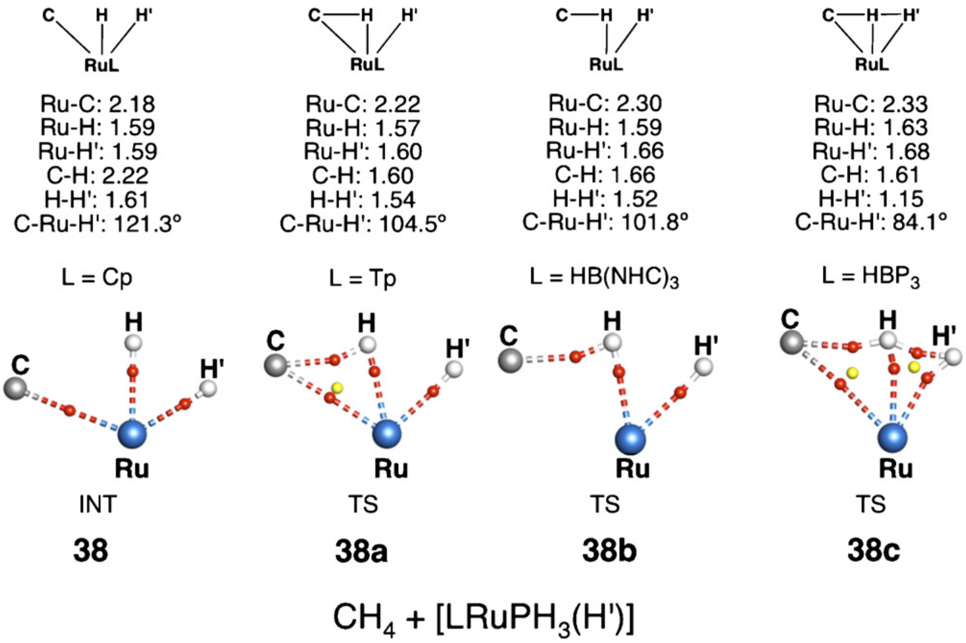

Fig. 15. Optimized geometric parameters and bonding patterns for **38** (L = Cp), **38a** (L = Tp), **38b** (L = HB(NHC)$_3$), and **38c** (L = HBP$_3$). The distances listed are in angstroms and the angles in degrees.

The characteristic RCP that is found inside the four-center coordinates of **1** was not located in the gradient field in the STO-3G basis; instead, a BCP was located along the Sc–H coordinates with two RCPs nearly overlapping this BCP on both sides. Because of this discrepancy in bonding patterns for this small basis, we do not report the values for the RCP density and the geometric parameters at this level.

Basis set effects are more prominent for the densities of the CPs than for the relative locations of the CPs in the density. However the STO-*n*G ($n = 3, 6$) basis sets performed poorly in describing both the value of the density at these CPs and their relative locations. While the values of the density at the CPs are slightly smaller at the WTBS level, the relative coordinates of the CPs are similar for this basis set to those of the larger basis sets.

3.3.3. Density functionals

In Table 6, we report the metric and density values of the three CPs of **1** from twelve DFs. We used the B3LYP/DZP optimized coordinates of **1** and assigned the cc-pVDZ basis sets to the scandium, carbon, and transferring hydrogen atoms while the methyl and Cp hydrogen atoms were assigned the D95 basis set. This level of basis was chosen as it was shown in the previous table to return accurate values for these CPs so any effect of the DF will be readily apparent.

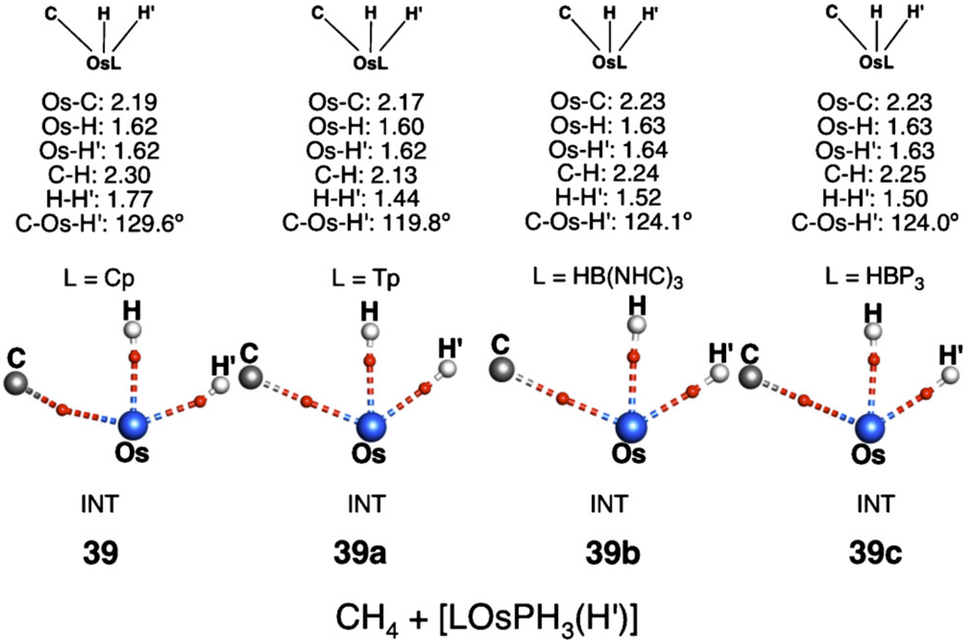

Fig. 16. Optimized geometric parameters and bonding patterns for **39** (L = Cp), **39a** (L = Tp), **39b** (L = HB(NHC)$_3$), and **39c** (L = HBP$_3$). The distances listed are in angstroms and the angles in degrees.

Table 5
Density and metric data for the **B**, **B**′ and **R** CPs of **1** for the basis sets listed

Basis set	CP ρ (e/bohr^3)			Metric data (Å)			∠Sc–**B**–C (°)
	B	**B**′	**R**	**B**	**R**	**B**–**R**	
STO-3G	0.04812	0.13143	NA	NA	NA	NA	163.3
STO-6G	0.04789	0.13134	0.04643	1.114	1.019	0.556	163.8
WTBS	0.04981	0.12846	0.04607	1.158	1.136	0.605	168.2
3-21G	0.05104	0.12770	0.04763	1.159	1.144	0.622	167.7
6-31G	0.04991	0.12842	0.04677	1.161	1.138	0.597	167.4
6-31G*	0.05081	0.12845	0.04724	1.164	1.139	0.598	167.5
pVDZ	0.05039	0.12831	0.04674	1.158	1.136	0.605	168.0
TZV	0.05099	0.12828	0.04750	1.155	1.135	0.599	167.7
VDZ	0.05015	0.12835	0.04642	1.160	1.137	0.605	168.2
VTZ	0.05132	0.12840	0.04779	1.157	1.135	0.600	167.8
Wachters + f	0.05270	0.12847	0.04782	1.159	1.137	0.612	168.8
cc-pVDZ	0.05204	0.12831	0.04783	1.159	1.135	0.605	168.1
aug-cc-pVDZ	0.05213	0.12850	0.04776	1.159	1.136	0.607	168.3
cc-pVDZ-DK	0.05221	0.12853	0.04777	1.160	1.137	0.608	168.4
cc-pVTZ	0.05205	0.12836	0.04810	1.160	1.137	0.603	167.9
cc-pVQZ	0.05286	0.12822	0.04821	1.157	1.136	0.606	168.3
ANO	0.05269	0.12826	0.04794	1.159	1.136	0.609	168.5

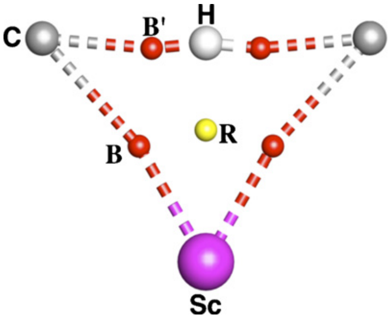

Fig. 17. Atomic and CP definitions for the following analyses of **1**.

The change in exchange and correlation functionals exhibits little effect on these values in comparing the data of the first four functionals. The radial distance of **B** (from the scandium coordinates) shortens when exact exchange is admixed into the DF, this distance continues to shorten as more exact exchange is included. Conversely, the radial distance of **B**′ (from the carbon coordinates) increases as more exact exchange is admixed into the functional; the corresponding parameter for **R** remains essentially unchanged. The values of the density at these CPs are also insensitive to the DF. Last we tested two meta density functionals (BB95, TPSS) and a hybrid density functional (MPWLYP1M) and observe minor differences between the values calculated with these functionals.

Table 7
Optimized geometric parameters for **1** optimized with four basis sets assigned to scandium

Basis set	Metric data			
	r(Sc–C) (Å)	**r**(Sc–H) (Å)	**r**(C–H) (Å)	∠C–Sc–C (°)
WTBS	2.409	1.891	1.438	73.3
Wachters + f	2.408	1.899	1.441	73.5
cc-pVDZ	2.408	1.897	1.440	73.4
LANL2mDZ(f)	2.409	1.896	1.441	73.5

3.3.4. Full optimization

Species **1** was individually optimized with four different basis sets assigned to the scandium (WTBS, Wachters + f, cc-pVDZ, and LANL2mDZ) and the electron densities of these optimized geometries were analyzed with Bader's analysis. The basis sets assigned to the carbon and hydrogen atoms of DZP remained the same for these optimizations. The optimized geometric parameters are presented in Table 7.

Interestingly, the optimized geometric parameters of **1** are similar between these four basis sets. The C–H distance that was calculated at the WTBS level is slightly smaller than the other three values, and this distance corresponds to the slightly smaller C–Sc–C angle at this same level.

The corresponding metric data and density values for the CPs for these four geometries of **1** are reported in Table 8. Minor differences between the density values and radial distances of these CPs are observed. The distance of **R** from the scandium center calculated at the Wachters + f level is ~0.1 Å longer than those calculated at the

Table 6
Density and metric data for **B**, **B**′ and **R** of **1** for the density functionals listed

Functional	CP ρ (e/bohr^3)			Metric data (Å)			∠Sc–**B**–C (°)
	B	**B**′	**R**	Sc–**B**	C–**B**′	Sc–**R**	
BLYP	0.05146	0.12771	0.04803	1.164	0.958	1.137	167.9
BPW91	0.05206	0.12697	0.04846	1.164	0.961	1.138	167.8
mPWPW91	0.05200	0.12691	0.04844	1.164	0.961	1.138	167.7
PBE	0.05211	0.12671	0.04855	1.164	0.962	1.139	167.7
B3LYP	0.05204	0.12831	0.04783	1.159	0.966	1.135	168.1
B3PW91	0.05251	0.12768	0.04817	1.159	0.968	1.136	168.0
MPW0	0.05262	0.12777	0.04814	1.158	0.970	1.136	168.0
PBE0	0.05271	0.12760	0.04823	1.158	0.970	1.136	167.9
BH&HLYP	0.05252	0.12944	0.04741	1.152	0.977	1.133	168.2
BB95	0.05137	0.12634	0.04806	1.164	0.959	1.138	167.9
TPSS	0.05172	0.12768	0.04798	1.162	0.960	1.137	168.0
MPWLYP1M	0.05162	0.12803	0.04781	1.162	0.960	1.137	168.3

Table 8
Metric data of the CPs and corresponding densities for **1** optimized with each basis set listed

Basis set	**B**		**B′**		**R**		∠Sc–**B**–C (°)
	r[a] (Å)	ρ (e/bohr^3)	**r**[b] (Å)	ρ (e/bohr^3)	**r**[a] (Å)	ρ (e/bohr^3)	
WTBS	1.157	0.05012	0.965	0.12905	1.134	0.04653	168.0
Wachters + f	1.159	0.05313	0.964	0.12578	1.144	0.04611	166.0
cc-pVDZ	1.159	0.05210	0.965	0.12853	1.136	0.04768	168.4
LANL2mDZ(f)	1.157	0.05010	0.964	0.12912	1.134	0.04653	168.0

[a] Relative to scandium coordinates.
[b] Relative to carbon coordinates.

other levels, and the Sc–**B**–C angle is 2° smaller at this same level in the basis. Interestingly, the values returned with WTBS assigned to scandium are similar to those values calculated at higher levels of theory when the molecule was optimized with this basis set.

4. Conclusions

We have identified in total seven bonding patterns by analyzing midpoint species along the reaction coordinates of the reactions described above. On the sole basis of geometric parameters of these TM species, the bonding patterns cannot be determined *a priori*, and Bader's analysis is helpful in characterizing the bonding patterns of these model complexes (Fig. 4). The transferring hydrogen does not interact with the metal center in the "classic" σBM mechanism (e.g. **1**, **2**, **3**). For the other "classic" mechanism, OA/RE, the hydrogen can bond to the metal in the TS (e.g. **8**) and forms a full single bond in the oxidized intermediate (e.g. **6**, **9**). Differing degrees of connectivity have been identified in TSs for hydrogen transfer; thus connectivity varies in these reactions. In general, those metal centers that have d electrons available to participate in hydrogen transfer interact with the transferring hydrogen during this reaction.

Acknowledgements

This work was supported by grants from the NSF (CHE-0518074, CHE-0541587, and DMS-0216275) and Welch Foundation (A0648).

References

[1] (a) K. Godula, D. Sames, Science 312 (2006) 67;
(b) A.E. Shilov, G.B. Shul'pin, Chem. Rev. 97 (1997) 2879;
(c) K.I. Goldberg, A.S. Goldman (Eds.), Activation and Functionalization of C–H Bonds, Oxford University Press, Washington, DC, 2004, p. 1.
[2] S. Sakaki, Theoretical studies of C–H σ-bond activation and related reactions by transition-metal complexes, in: G. Frenking (Ed.), Theoretical Aspects of Transition Metal Catalysis: Topics in Organometallic Chemistry, vol. 12, Springer, New York, 2005, p. 3.
[3] (a) P.L. Watson, J. Am. Chem. Soc. 105 (1983) 6491;
(b) P.L. Watson, G.W. Parshall, Acc. Chem. Res. 18 (1985) 51;
(c) M.E. Thompson, S.M. Baxter, A.R. Bulls, B.J. Burger, M.C. Nolan, B.D. Santarsiero, W.P. Schaefer, J.E. Bercaw, J. Am. Chem. Soc. 109 (1987) 203;
(d) J.W. Bruno, T.J. Marks, V.W. Day, J. Am. Chem. Soc. 104 (1982) 7357;
(e) C.M. Fendrick, T.J. Marks, J. Am. Chem. Soc. 106 (1984) 2214;
(f) C.M. Fendrick, T.J. Marks, J. Am. Chem. Soc. 108 (1986) 425;
(g) T. Ziegler, E. Folga, A. Berces, J. Am. Chem. Soc. 115 (1993) 636;
(h) E. Folga, T. Ziegler, Can. J. Chem. 70 (1992) 333.
[4] (a) M.L.H. Green, P.J. Knowles, J. Chem. Soc. Chem. Commun. (1970) 1677;
(b) J.K. Hoyano, W.A.G. Graham, J. Am. Chem. Soc. 104 (1982) 3723;
(c) A.H. Janowicz, R.G. Bergman, J. Am. Chem. Soc. 104 (1982) 352;
(d) B.A. Arndsten, R.G. Bergman, Science 270 (1995) 1970;
(e) D.L. Strout, S. Zarić, S. Niu, M.B. Hall, J. Am. Chem. Soc. 118 (1996) 6068;
(f) S. Niu, M.B. Hall, J. Am. Chem. Soc. 120 (1998) 6169;
(g) S. Niu, M.B. Hall, Chem. Rev. 100 (2000) 353;
(h) S.R. Klei, T.D. Tilley, R.G. Bergman, J. Am. Chem. Soc. 122 (2000) 1816.
[5] (a) C.E. Webster, Y. Fan, M.B. Hall, D. Kunz, J.F. Hartwig, J. Am. Chem. Soc. 125 (2003) 858;
(b) J.F. Hartwig, K.S. Cook, M. Hapke, C.D. Incarvito, Y. Fan, C.E. Webster, M.B. Hall, J. Am. Chem. Soc. 127 (2005) 2538.
[6] S.M. Ng, W.H. Lam, C.C. Mak, C.W. Tsang, G. Jia, Z. Lin, C.P. Lau, Organometallics 22 (2003) 641.
[7] W.H. Lam, G. Jia, Z. Lin, C.P. Lau, O. Eisenstein, Chem. Eur. J. 9 (2003) 2775.
[8] (a) W.H. Lam, Z. Lin, Organometallics 22 (2003) 473;
(b) Z. Lin, Coord. Chem. Rev. 251 (2007) 2280.
[9] (a) J. Oxgaard, R.P. Muller, W.A. Goddard III, R.A. Periana, J. Am. Chem. Soc. 126 (2004) 352;
(b) J. Oxgaard, W.A. Goddard III, J. Am. Chem. Soc. 126 (2004) 442;
(c) J. Oxgaard, R.A. Periana, W.A. Goddard III, J. Am. Chem. Soc. 126 (2004) 11658.
[10] T. Matsumoto, D.J. Taube, R.A. Periana, H. Taube, H. Yoshida, J. Am. Chem. Soc. 122 (2000) 7414.
[11] M. Lail, B.N. Arrowood, T.B. Gunnoe, J. Am. Chem. Soc. 125 (125) (2003) 7506.
[12] R.N. Perutz, S. Sabo-Etienne, Angew. Chem. Int. Ed. 46 (2007) 2578.
[13] (a) R.H. Crabtree, Angew. Chem. Int. Ed. Engl. 32 (1993) 789;
(b) C. Hall, R.N. Perutz, Chem. Rev. 96 (1996) 3125.
[14] R.F.W. Bader, Atoms in Molecules, A Quantum Theory, Oxford University Press, Ithaca, NY, 1990, pp. 1–438.
[15] B.A. Vastine, M.B. Hall, J. Am. Chem. Soc. 129 (2007) 12068.
[16] R.G. Parr, W. Yang, Density Functional Theory of Atoms and Molecules, Oxford University Press, New York, 1989, pp. 1–333.
[17] M.J. Frisch, G.W. Trucks, H.B. Schlegel, G.E. Scuseria, M.A. Robb, J.R. Cheeseman, J.A. Montgomery Jr., T. Vreven, K.N. Kudin, J.C. Burant, J.M. Millam, S.S. Iyengar, J. Tomasi, V. Barone, B. Mennucci, M. Cossi, G. Scalmani, N. Rega, G.A. Petersson, H. Nakatsuji, M. Hada, M. Ehara, K. Toyota, R. Fukuda, J. Hasegawa, M. Ishida, T. Nakajima, Y. Honda, O. Kitao, H. Nakai, M. Klene, X. Li, J.E. Knox, H.P. Hratchian, J.B. Cross, V. Bakken, C. Adamo, J. Jaramillo, R. Gomperts, R.E. Stratmann, O. Yazyev, A.J. Austin, R. Cammi, C. Pomelli, J.W. Ochterski, P.Y. Ayala, K. Morokuma, G.A. Voth, P. Salvador, J.J. Dannenberg, V.G. Zakrzewski, S. Dapprich, A.D. Daniels, M.C. Strain, O. Farkas, D.K. Malick, A.D. Rabuck, K. Raghavachari, J.B. Foresman, J.V. Ortiz, Q. Cui, A.G. Baboul, S. Clifford, J. Cioslowski, B.B. Stefanov, G. Liu, A. Liashenko, P. Piskorz, I. Komaromi, R.L. Martin, D.J. Fox, T. Keith, M.A. Al-Laham, C.Y. Peng, A. Nanayakkara, M. Challacombe, P.M.W. Gill, B. Johnson, W. Chen, M.W. Wong, C. Gonzalez, J.A. Pople, Gaussian 03, Revision D. 02, Gaussian, Inc., Wallingford, CT, 2004.
[18] A.D. Becke, J. Chem. Phys. 98 (1993) 5648.
[19] C. Lee, W. Yang, R.G. Parr, Phys. Rev. B: Condens. Matter Mater. Phys. 37 (1988) 785.
[20] (a) J. Manson, C.E. Webster, L.M. Pérez, M.B. Hall, JIMP 2 Version 0. 091 (Built for Windows PC), Department of Chemistry, Texas A&M University, College Station, TX, 2006 (available at http://www.chem.tamu.edu/jimp2/index.html);
(b) M.B. Hall, R.F. Fenske, Inorg. Chem. 11 (1972) 768.
[21] AIM2000 designed by Friedrich Biegler-König, University of Applied Sciences, Bielefeld, Germany (https://www.aim2000.de/).
[22] P.J. Hay, W.R. Wadt, J. Chem. Phys. 82 (1985) 270.
[23] M. Couty, M.B. Hall, J. Comp. Chem. 17 (1996) 1359.
[24] (a) T.H. Dunning Jr., J. Chem. Phys. 90 (1989) 1007;
(b) D.E. Woon, T.H. Dunning Jr., J. Chem. Phys. 98 (1993) 1358.
[25] T.H. Dunning Jr., P.J. Hay, in: H.F. Schaefer III (Ed.), Modern Theoretical Chemistry, Plenum, New York, 1996, p. 1.
[26] D. Andrae, U. Haussermann, M. Dolg, H. Stoll, H. Preuss, Theor. Chim. Acta 77 (1990) 123.
[27] S. Huzinaga, B. Miguel, J. Chem. Phys. Lett. 175 (1990) 289.
[28] (a) W.J. Hehre, R.F. Stewart, J.A. Pople, J. Chem. Phys. 51 (1969) 2657;
(b) J.B. Collins, P.v.R. Schleyer, J.S. Binkley, J.A. Pople, J. Chem. Phys. 64 (1976) 5142.
[29] J.S. Binkley, J.A. Pople, W.J. Hehre, J. Am. Chem. Soc. 102 (1980) 939.
[30] V.A. Rassolov, J.A. Pople, M.A. Ratner, T.L. Windus, J. Chem. Phys. 109 (1998) 1223.
[31] A. Schäfer, H. Horn, R. Ahlrichs, J. Chem. Phys. 97 (1992) 2571.
[32] A. Schäfer, C. Huber, R. Ahlrichs, J. Chem. Phys. 100 (1994) 5829.
[33] F. Weigend, M. Haser, H. Patzelt, R. Ahlrichs, Chem. Phys. Lett. 294 (1998) 143.
[34] N.B. Balabanov, K.A. Peterson, J. Chem. Phys. 123 (2005) 064107.
[35] A.J.H. Wachters, J. Chem. Phys. 52 (1970) 1033;
C.W. Bauschlicher Jr., S.R. Langhoff, H. Partirdge, L.A. Barnes, J. Chem. Phys 91 (1989) 2399 [F-exponents].
[36] C.W. Bauschlicher Jr., Theor. Chim. Acta 92 (1995) 183.
[37] A.D. Becke, Phys. Rev. A 38 (1988) 3098.

[38] A.D. Becke, J. Chem. Phys. 98 (1993) 1372.
[39] (a) C. Adamo, V. Barone, J. Chem. Phys. 108 (1998) 664;
(b) J.P. Perdew, in: P. Ziesche, H. Eschig (Eds.), Electronic Structure of Solids, Akademie Verlag, Berlin, 1991.
[40] A.D. Becke, J. Chem. Phys. 104 (1996) 1040.
[41] (a) J.P. Perdew, K. Burke, M. Ernzerhof, Phys. Rev. Lett. 77 (1996) 3865;
(b) J.P. Perdew, K. Burke, M. Ernzerhof, Phys. Rev. Lett. 78 (1997) 1396.
[42] J. Tao, J.P. Perdew, V.N. Staroverov, G.E. Scuseria, Phys. Rev. Lett. 91 (2003) 146401.
[43] N.E. Schultz, Y. Zhao, D.G. Truhlar, J. Phys. Chem. A 109 (2005) 11127.
[44] B.A. Vastine, C.E. Webster, M.B. Hall, J. Chem. Theory Comput. 3 (2007) 2268.
[45] X. Hu, I. Castro-Rodriguez, K. Meyer, Organometallics 22 (2003) 3016.
[46] (a) J.C. Peters, J.D. Feldman, T.D. Tilley, J. Am. Chem. Soc. 121 (1999) 9871;
(b) J.D. Feldman, J.C. Peters, T.D. Tilley, Organometallics 21 (2002) 4050;
(c) J.D. Feldman, J.C. Peters, T.D. Tilley, Organometallics 21 (2002) 4065.